Impacts of Spatial Heterogeneity and Temporal Non-Stationarity on Intensity-Duration-Frequency Estimates—A Case Study in a Mountainous California-Nevada Watershed

Huiying Ren [1,]*, Z. Jason Hou [1], Mark Wigmosta [1], Ying Liu [2] and L. Ruby Leung [2]

[1]   Hydrology, Pacific Northwest National Laboratory, Richland, WA 99354, USA;
      Zhangshuan.Hou@pnnl.gov (Z.J.H.); Mark.Wigmosta@pnnl.gov (M.W.)
[2]   Earth Systems Analysis and Model, Pacific Northwest National Laboratory, Richland, WA 99354, USA;
      Ying.Liu@pnnl.gov (Y.L.); Ruby.Leung@pnnl.gov (L.R.L.)
*   Correspondence: Huiying.Ren@pnnl.gov; Tel.: +1-509-372-4088

check for
updates

Abstract: Changes in extreme precipitation events may require revisions of civil engineering standards to prevent water infrastructures from performing below the designated guidelines. Climate change may invalidate the intensity-duration-frequency (IDF) computation that is based on the assumption of data stationarity. Efforts in evaluating non-stationarity in the annual maxima series are inadequate, mostly due to the lack of long data records and convenient methods for detecting trends in the higher moments. In this study, using downscaled high resolution climate simulations of the historical and future periods under different carbon emission scenarios, we tested two solutions to obtain reliable IDFs under non-stationarity: (1) identify quasi-stationary time windows from the time series of interest to compute the IDF curves using data for the corresponding time windows; (2) introduce a parameter representing the trend in the means of the extreme value distributions. Focusing on a mountainous site, the Walker Watershed, the spatial heterogeneity and variability of IDFs or extremes are evaluated, particularly in terms of the terrain and elevation impacts. We compared observations-based IDFs that use the stationarity assumption with the two approaches that consider non-stationarity. The IDFs directly estimated based on the traditional stationarity assumption may underestimate the 100-year 24-h events by 10% to 60% towards the end of the century at most grids, resulting in significant under-designing of the engineering infrastructure at the study site. Strong spatial heterogeneity and variability in the IDF estimates suggest a preference for using high resolution simulation data for the reliable estimation of exceedance probability over data from sparsely distributed weather stations. Discrepancies among the three IDFs analyses due to non-stationarity are comparable to the spatial variability of the IDFs, underscoring a need to use an ensemble of non-stationary approaches to achieve unbiased and comprehensive IDF estimates.

Keywords: IDF; heterogeneity; non-stationarity; extreme precipitation; high-resolution and bias-corrected regional simulations; climate change

1. Introduction

Intensity-duration-frequency (IDF) curves have been widely used in water resources engineering to support the planning and design of hydrological infrastructure and facilities in flood risk and water management [1,2]. As rainfall-runoff modeling is typically used for flood estimation [3], IDF curves at the watershed scale are critical inputs to watershed models for designing storm water conveyance and flood control structures [4,5].

Developing IDF curves generally requires long term stationary annual maximum rainfall time series data. However, precipitation intensity is projected to generally increase with global warming as the atmosphere holds more moisture at higher temperatures (e.g., with the projected poleward shifts of the storm tracks [6] and expansion of the subtropical high pressure systems [7] with warming, precipitation may increase in high latitude regions but decrease in the subtropical land regions, which may influence the regional patterns of extreme precipitation). Hence, with climate change, the historical extremes cannot be used to characterize the extremes of the future [8]. A substantial increase in extreme precipitation has already been observed in recent decades not only in the United States [9,10] but also in Canada [11], Brazil [12], South Korea [13], India [14], African cities [15] and other regions worldwide [16]. What has already been observed as well as projected changes suggest that with global warming, extreme storm events may occur more frequently and in greater severity [17,18].

Motivated by the need to consider the impacts of climate change on extreme precipitation, this study is designed to evaluate, distinguish, and compare the impacts of temporal non-stationarity (e.g., trending) and spatial heterogeneity (e.g., terrain/elevation) on IDF analyses. A stationary system is ergodic [19,20]. If trending is not negligible, non-stationarity needs to be considered in the process as ergodicity cannot hold [21]. On the other hand, non-stationarity cannot be misused to underestimate the risk [22]. Quasi-stationary time windows are great choices without violating either the stationary assumption or any long-term trending. Combing two alternative approaches for addressing the non-stationary issues helps to develop more reliable IDFs for predicting precipitation intensity extremes during the next century. To achieve our goal, simulation outputs related to the Walker River Basin located in the Western United States from a regional climate model are used to provide long time series of precipitation spanning from 1975–2100 for analysis in this study. The long time series allow the impact of temporal non-stationarity in precipitation on IDFs to be evaluated. Furthermore, with the high-resolution climate simulations, the impact of spatial heterogeneity can be quantified for comparison with the impact of temporal non-stationarity [23]. In this study, the author investigated the annual maximum time series with 6- and 24-h durations extracted from relatively high spatial resolution precipitation datasets at each simulation grid. Detailed geostatistical modeling and mapping of extreme precipitation intensity and exceedance probabilities were conducted, which enabled the revelation of their spatial patterns at the watershed scale. Our results can be used to inform the future development of IDF analyses to address potential over- and under-design issues in hydrological infrastructure.

2. Materials and Methods

2.1. Research Area

The present study is focused on the Walker River Basin as shown in Figure 1. The southern boundary of the Walker River drainage basin forms the northern border of the Yosemite National Park. Walker Lake is one of the few perennial, natural terminal lakes in west-central Nevada at the endpoint of the Walker River system of Nevada and California. Terminal lakes are the terminus of surface-water drainage in topographically closed basins. Water uses in the basin have been evaluated in scientific studies to maintain a healthy agricultural economy by the ecosystems and recreational uses of the Walker Lake [24]. However, IDF analyses are not available to provide guidance on designing hydrological infrastructure in this watershed.
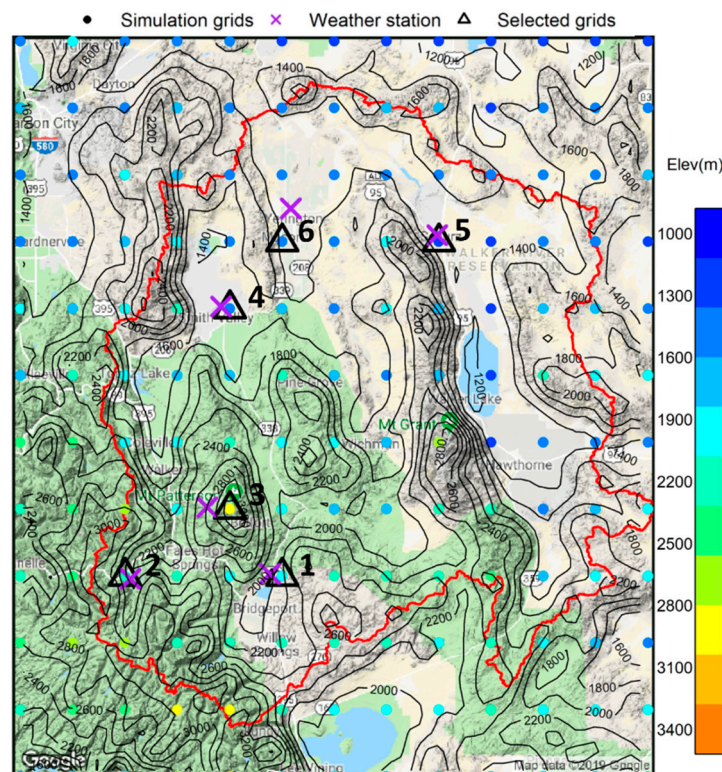
Figure 1. Location of the study area on a google map. The red line is the boundary of the Walker River Basin. The dots are the centroid locations of the bias-corrected Regional Earth System Model (RESM) data, with different colors corresponding to the elevations of the grid centroids. The altitude contour in this study domain is illustrated in black lines. The indexed black triangle boxes correspond to the six selected grids with distinct topography for illustration in the results section. The purple cross symbols represent the closest weather stations to each selected grid.

2.2. Method

This study used model outputs from the Regional Earth System Model (RESM) [25,26] developed at the Pacific Northwest National Laboratory (PNNL) based on the Weather Research and Forecasting (WRF) model [27] coupled with the Community Land Model (CLM) [28] through the flux coupler (CPL7) of the Community Earth System Model (CESM) [29] that facilitates an exchange of fluxes in a conservative manner. RESM was applied to a North American domain at 20 km grid resolution, with lateral boundary conditions and sea surface temperature and sea ice data provided by CESM. The CESM simulations are part of the Coupled Model Intercomparison Project Phase 5 (CMIP5) archive [30]. Driven by CESM boundary conditions, the RESM historical simulation covers the period of 1975–2004. Two future projections were simulated to cover the period of 2005–2100 following two representative concentration pathways (RCP), RCP4.5 and RCP8.5, corresponding to an emission mitigation scenario and a business-as-usual scenario, respectively. The bias correction spatial disaggregation (BCSD) method of Wood et al. (2004) was applied to the RESM historical and future simulations to provide bias-corrected time series of precipitation at a 0.125° latitude-longitude grid. Precipitation time series were then extracted from the bias-corrected RESM outputs to the $13 \times 12 = 156$ grid cells, with a latitude range of [37.9375, 39.3125] and a longitude range of [−119.8125, −118.3125], covering the Walker River Basin (see Figure 1). Among all the numerical grids, six were found to have adjacent weather stations, representing a variety of terrain and potentially different climate conditions. IDF analyses were performed using the bias-corrected RESM outputs for each grid and compared with IDFs obtained using data from weather stations at six selected grid cells.

2.3. Trend Analysis

Trend analysis can be conducted to evaluate the non-stationarity in the historical and future precipitation extremes. In this study, trend analyses including the Mann–Kendall (MK) test and Sen's slope analysis were conducted for the annual maximum series (AMS) of precipitation at each grid for different durations (6- and 24-h, which are the most commonly used event durations in extreme precipitation studies) and climate scenarios. The Mann–Kendall (MK) test [31] is a nonparametric statistical test for detecting trends in a time series. It can identify trends in the time series without assuming linearity [32]. The MK method has been widely-used for assessing the significance of trends in hydroclimatic time series data such as rainfall, temperature and stream flow [33–38]. Sen [39] developed a nonparametric procedure to estimate the slope of trends using linear model through pairs of sample points, which has become the classical method used to quantify trends in time series in hydrometeorology [40–42].

2.4. Quasi-Stationary and Non-Stationary IDFs

To obtain reliable IDFs, two solutions can be implemented: (1) identify quasi-stationary time windows from the time series of interest [43,44] and compute the IDF curves using data for the corresponding time windows; (2) introduce a parameter representing the trend in the means of the extreme value distributions [45–48]. Here, we adopt these approaches and derive both quasi-stationary and non-stationary IDFs for the study site. Extreme value theory has provided a framework to analyze the climate extremes and IDFs [49–51], which usually involves the fitting of generalized extreme value (GEV) distributions. The GEV distribution family consists of Gumbel, Fréchet and Weibull distributions. The standard cumulative distribution of GEV can be expressed as:

$$F(x|\mu,\ \sigma,\ \xi) = \exp\left\{-\left(1 + \xi\left(\frac{x-\mu}{\sigma}\right)\right)^{\frac{-1}{\xi}}\right\},\tag{1}$$

The GEV distribution is flexible for modeling different behaviors of extremes with three distribution parameters: the location parameter μ, the scale parameter σ and shape parameter ξ. In order to represent a dynamic distribution, the location and scale parameters can be assumed to be linear functions of time to account for non-stationarity, with the shape parameter kept constant [52,53]. Then, μ and σ can be defined as

$$x_t = \mu_a + K_T \sigma_a,\tag{2}$$

$$\sigma(t) = \sigma_1 t + \sigma_0,\tag{3}$$

where t is the time in years, x_t denotes the intensity of the T-year return period event, K_T is the frequency factor, μ_a and σ_a are the mean and the standard deviation of the set of AMS, respectively.

For the simulated 6- and 24-h AMS under both climate scenarios at each modeling grid, GEV fitting was exanimated and the shape parameter ξ was generally found to be close to 0, which corresponds to the extreme value type I (EV1) distribution [54], which is also called the Gumbel distribution. Gumbel distribution is recommended by a number of studies as a good choice for developing IDFs [8,15,54–56]. After carefully examining the quasi-stationary window, EV1/Gumbel is applied for developing IDFs for a 30-year time window. The corresponding lognormal regression equations are developed and used to estimate the events with 2-, 5-, 10-, 25-, 50-, and 100-year returning periods. The equation for fitting the Gumbel distribution to precipitation AMS for different return periods T is similar to Equation (2) [57–59], with the Chow's Lognormal frequency factor K_T developed by [60]:

$$K_T = \frac{-\sqrt{6}}{\pi}\left[0.5772 + \ln\left(\ln\left(\frac{T}{T-1}\right)\right)\right],\tag{4}$$

In a stationary process, it is assumed that the probabilistic attributes of extreme events are independent of time. In a non-stationary process, the parameters of the underlying distribution function are time dependent and the properties of the distribution would vary with time. The framework we adopted to obtain non-stationary IDFs is called Non-stationary Extreme Value Analysis (NEVA) developed by [61]. The NEVA framework is based on the GEV and successfully used in nonstationary IDF analysis [47,48,62]. A Bayesian inversion framework was adopted in NEVA to infer the uncertainty of the GEV distribution parameters estimation under non-stationary conditions to yield more realistic estimations [63]. NEVA generates a large number of realizations from the parameter joint posterior distribution using the Differential Evolution Markov Chain (DE-MC) [64–66], which utilizes the generic algorithm DE for global optimization over the parameter space with the Markov-Chain Monte Carlo (MCMC) sampling approach.

Considering the non-stationarity in the data, two types of IDFs (i.e., quasi-stationary time windows based vs. trending parameter introduced non-stationary) were developed at all the numerical grids. The first IDF approach involves identification of quasi-stationary time windows [67]. The Mann–Kendall (MK) test failure rate was used to identify quasi-stationary time windows during the study period, and the 30-year-long time windows were determined to be the most stationary with lowest failure rate compared to other window sizes (e.g., 10-, 15-, 20-, 40-, and 50-year). After determining the quasi-stationary window, the IDFs were calculated for 30-year time periods including the historical period (1975–2004) and three future periods: 2011–2040, 2041–2070, and 2071–2100, respectively. The second non-stationary IDF approach is to apply the NEVA framework to the AMS for the entire time period (1975–2100), with 5000 DE-MC posterior samples in the Bayesian calibration of IDF parameters. Both the quasi-stationary and non-stationary IDFs were evaluated at each grid location, for durations of 6 and 24 h, for the 2-, 5-, 10-, 25-, 50-, and 100-year return periods, and for both RCP4.5 and RCP8.5 climate scenarios.

### 2.5. Geostatistics: (Variogram and Kriging)

Geostatistics has been used to evaluate and model spatial random functions, particularly when spatial heterogeneity and correlation patterns exist. It contains a suite of statistical methods including adaptations of classical regression techniques to describe the spatial continuity of natural phenomena. These methods aim to solve for characterization of spatial attributes by employing mainly random models in a similar fashion to the way time series analysis characterizes temporal data [68,69]. A package for geostatistical analysis named geoR [70] is used in our study to fit the variogram model for IDFs to reveal the spatial pattern of extreme events in the whole watershed.

3. Results

Bias-corrected RESM simulations of precipitation time series were used for IDF analyses. Trend analyses were done for the 126-year record (1975–2100) at each grid for the 6- and 24-h precipitation events under the RCP4.5 and RCP8.5 climate scenarios, as shown in Figure 2. The size of each dot represents the value of Sen's Slope at a confidence level set to be 0.95. The overall trending is all positive (i.e., increasing precipitation intensity) for different events under both climate scenarios. Generally stronger trending is observed for 6-h events than 24-h ones. The Sen's slope analysis shows the large spatial heterogeneity in the temporal trends, and that trending is extremely strong in mountain areas (e.g., northwest, southwest and middle of the region).

As a comparison, the IDFs with the traditional stationary assumption from historical observations were obtained at six adjacent weather stations from the Hydrometeorological Design Studies Center of NOAA's National Weather Service. Differences in the IDFs are shown at the selected grids highlighted in Figure 1. A comparison of the IDFs taken directly from the weather stations where the IDFs were obtained by the quasi-stationary approach for the same time period reflects biases in simulating precipitation by RESM, which has its own biases in addition to being influenced by biases in CESM1.

Although bias correction has been applied to the RESM outputs, it focuses on removing biases for monthly mean precipitation so biases may still exist for short-duration precipitation extremes.
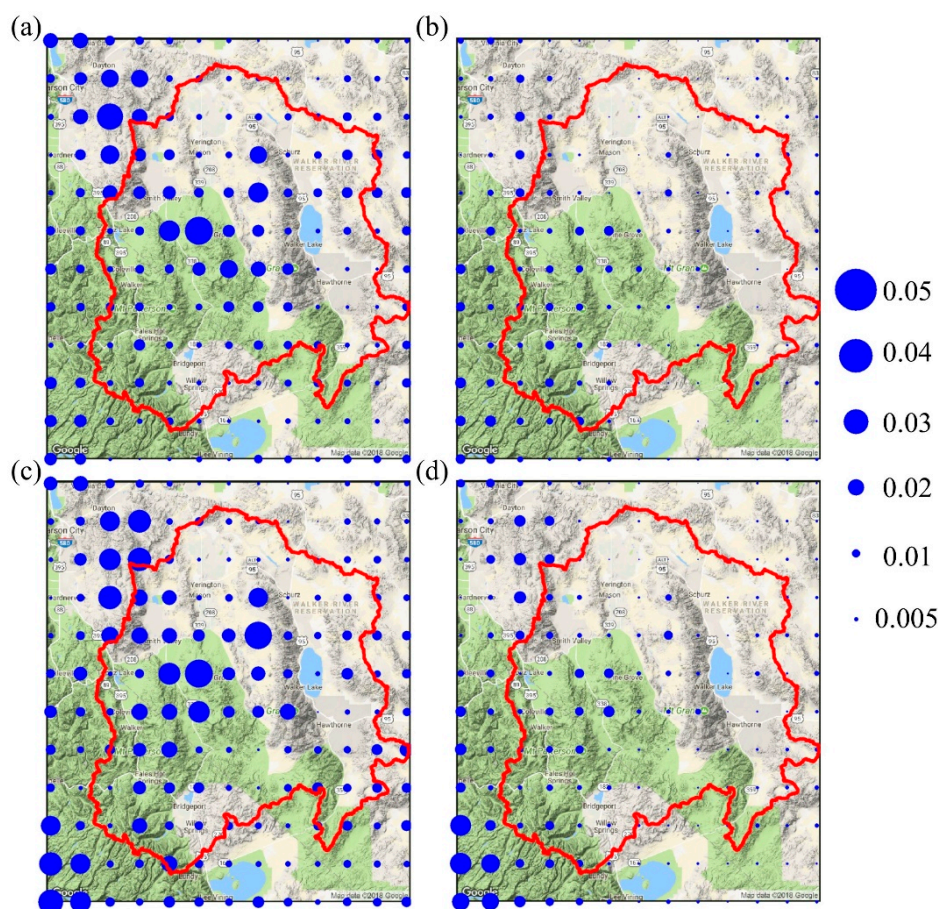

Figure 2. Spatial distributions of trending (Sen's slope) of 126-year precipitation annual maximum series (AMS) for (**a**) 6-h duration events under representative concentration pathway (RCP)4.5; (**b**) 24-h duration events under RCP4.5; (**c**) 6-h duration events under RCP8.5; and (**d**) 24-h duration events under RCP8.5.

The IDFs estimated by NEVA provide uncertainty bounds from the ensemble estimates based on DE-MC sampling. The medians and uncertainty bounds of the ensemble IDF estimates are shown in the boxplots in Figures 3 and 4, for events with durations of 6 and 24 h, respectively. The IDFs estimated using the non-stationarity approach is potentially the closest to the truth and used as references; the terms of "underestimation" and "overestimation" are used to describe the relative deviations. It is observed that IDFs estimated using the quasi-stationary approach for the historical period (1975–2004) suggests that the simulated precipitation during this time period is generally comparable with the six adjacent station observations. However, clear differences between IDFs obtained by different approaches are also noticeable at specific locations (e.g., grid 2) where the simulated precipitation is much lower than observed, especially for the high return periods. Such biases may be due to the lack of resolution in the model (20 km) as well as the gridded data (~12 km) that was used to bias correct the simulation in resolving the local conditions at Grid 2.

In general, the IDFs obtained from the weather stations deviate significantly from the ones estimated by the non-stationary approach and tend to underestimate the extremes especially for the 24-h duration events under both RCP4.5 and RCP8.5. For IDFs from the quasi-stationary approach, the estimates are higher for later time periods than earlier ones, although there are exceptions as they are confounded by spatial heterogeneity. For 6-h duration events (Figure 3), the IDFs based on

the quasi-stationary approach are within the uncertainty range given by the non-stationary NEVA approach; however, the IDFs from the weather stations with traditional stationarity assumption overestimate by more than 100% for most return periods at Grid 2. They also tend to overestimate for the shorter return periods at grids 5 and 6, and underestimate for grids 1, 3 and 4, especially under RCP8.5. For example, under RCP8.5, the IDFs from the weather stations overestimate by about 20% on Grid 5, and underestimate 25% at Grid 3 for 2- and 5-year return periods.
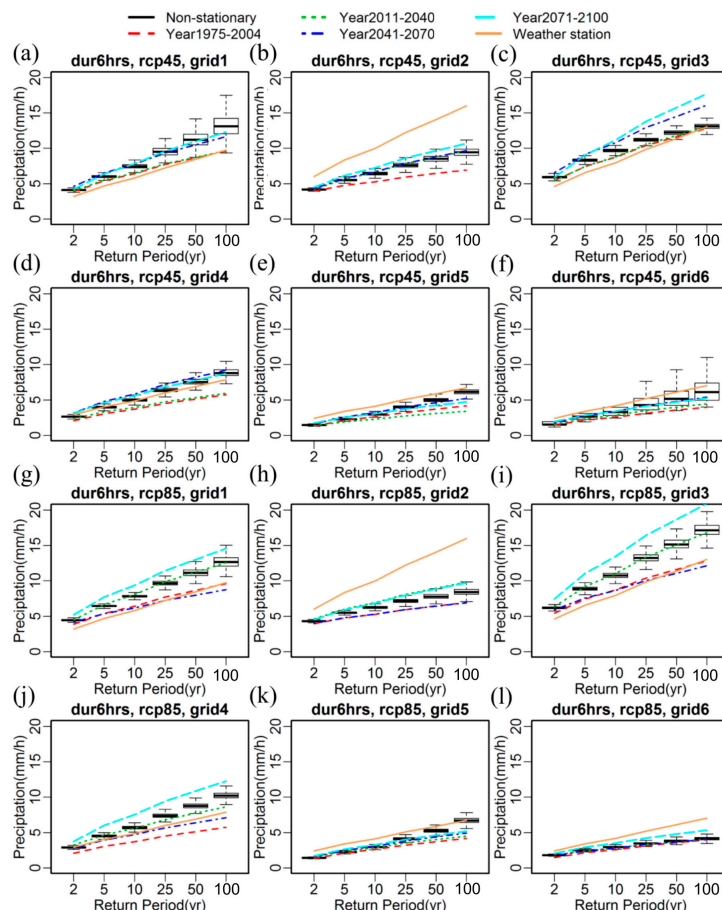
Figure 3. Example intensity-duration-frequencies (IDFs) at six selected grids for events with 6-h duration and 2-, 5-, 10-, 25-, 50-, and 100-year return periods, including the estimates from (1) the non-stationary NEVA approach, with the black boxplots showing the uncertainty bounds (here defined by the 1.5 interquartile range (IQR)) of IDF estimates using Non-Stationary Extreme Value Analysis (NEVA); (2) the quasi-stationary estimation during the four time periods: year 1975–2004, year 2011–2040, year 2041–2070 and year 2071–2100, as shown in red, green, blue, and cyan dashed lines, respectively, and (3) the adjacent weather stations (yellow solid lines). The panels (**a**–**f**) are for the RCP4.5 scenario; the panels (**g**–**l**) are for the RCP8.5 scenario.

Spatial heterogeneity in the IDFs is evident from our results. When the IDFs obtained from quasi- and non-stationary approaches are considered, the extreme precipitation magnitudes at grids 1 and 3 are remarkably higher than at other grids; for example, under the RCP8.5 scenario, the precipitation estimated by non-stationary approach at grid 3 for the 100-year return period is about 17 mm/h, which is two or three times as high as it is at grids 2, 4, 5 and 6. The elevation of grid 3 is the highest (~3400 m) among the entire region and corresponds to the highest precipitation intensities. Grids 4, 5 and 6 are at relatively lower elevations (~1600 m) and have lower precipitation intensities, although their IDFs using quasi-stationary and non-stationary approaches do show different patterns (e.g., different slopes and uncertainty bounds). These differences might be attributed to the weather

and topographic conditions of the surrounding area. The IDFs from the quasi-stationary approach in the future time window of year 2071–2100 are within or very close to the bounds given by the IDFs from NEVA under both climate scenarios. The largest deviation (~30%) between the two IDFs obtained by quasi-stationary at 2071–2100 and non-stationary approaches is observed at grid 3 under RCP4.5.
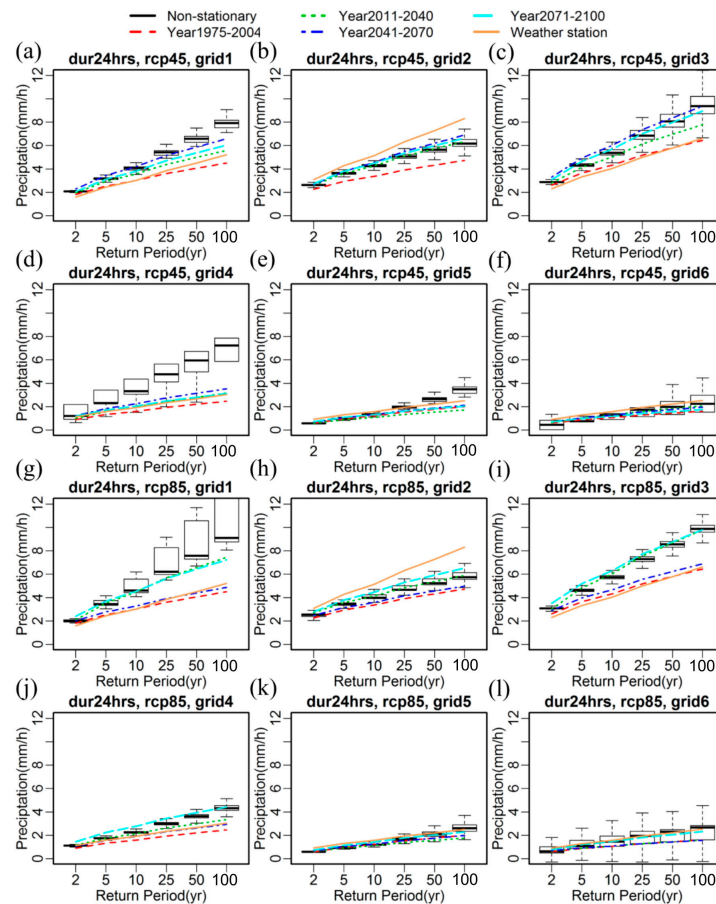

**Figure 4.** Example IDFs same as Figure 3, for 24-h durations.

For the 24-h duration IDFs in Figure 4, the differences between the traditional stationary IDFs with the quasi-stationary IDFs for the same historical period are clearly smaller than the differences for the 6-h duration IDFs. This is consistent with the bias correction using monthly mean data, which should have larger impacts on removing biases for longer duration than shorter duration events. The traditional stationary IDFs from the weather stations tend to underestimate for longer return periods at all the selected grids except for grid 2. Under the RCP4.5 scenario at grids 1, 4 and 5, the estimates by both traditional and quasi-stationary IDFs underestimate by up to ~60% for the 100-year return period. The quasi-stationary IDFs for both time periods 2041–2070 and 2071–2100 are comparable to the non-stationary ones at grids 2, 3, and 6; on the other hand, the traditional stationary IDFs overestimate by ~30% (~8 mm/h) at grid 2 and underestimate by ~30% (~6 mm/h) at grid 3 compared to the non-stationary IDFs, which yield an estimate of ~6 mm/h and 9 mm/h, respectively.

Under the RCP8.5 scenario, the traditional stationary IDFs underestimate by ~40% at grids 1, 3, and 4 for the 100-year return period, while the quasi-stationary IDF estimates for the period 2071–2100 match the non-stationary ones at all the selected grids. The largest deviation (~15% from the non-stationary estimation median) is observed at grid 1. The uncertainty bounds of the non-stationary IDFs are generally larger with higher emission inputs at all grids, and these bounds increase with the return period.

The above comparison shows a general agreement between the two non-stationary IDF approaches, although at a few locations (e.g., grids 1) larger deviations are observed. Such deviations might be statistically insignificant given the corresponding large uncertainty bounds in the estimated IDFs. In the following section, we fully evaluate the differences using the two non-stationary IDF analyses approaches, by looking at both deviations from the mean/median estimates and the uncertainty bounds of IDFs, for all time periods of study, at different spatial locations, for the 6-h and 24-h events of various return periods, under the two climate scenarios.

The differences between non-stationary and quasi-stationary IDFs over the entire watershed are illustrated in Figures 5 and 6, where the boxplots show the distributions of relative difference percentage, computed as (non-stationary–quasi-stationary)/non-stationary*100%, at each numerical grid. Overall, in the majority of grids, the quasi-stationary framework produced IDFs that might underestimate the risk of extreme events for both short and long durations since the differences are positive for most boxplots. For the RCP4.5 scenario in Figure 5, the quasi-stationary window 2071–2100 has the smallest differences compared with the non-stationary IDF because the mean values of the difference approach zero for all return periods. However, under the RCP8.5 scenario, the mean values of differences are all positive, e.g., the relative differences in non-stationary IDFs for 24-h 100-year events are about 25% on average. The extra precipitation in a 24-h storm would cause a significant increase in flood peak. Another observation of the boxplots under both climate scenarios is that the uncertainty grows with the return period. Also, compared with the longer duration events, the uncertainty of shorter duration events is larger.
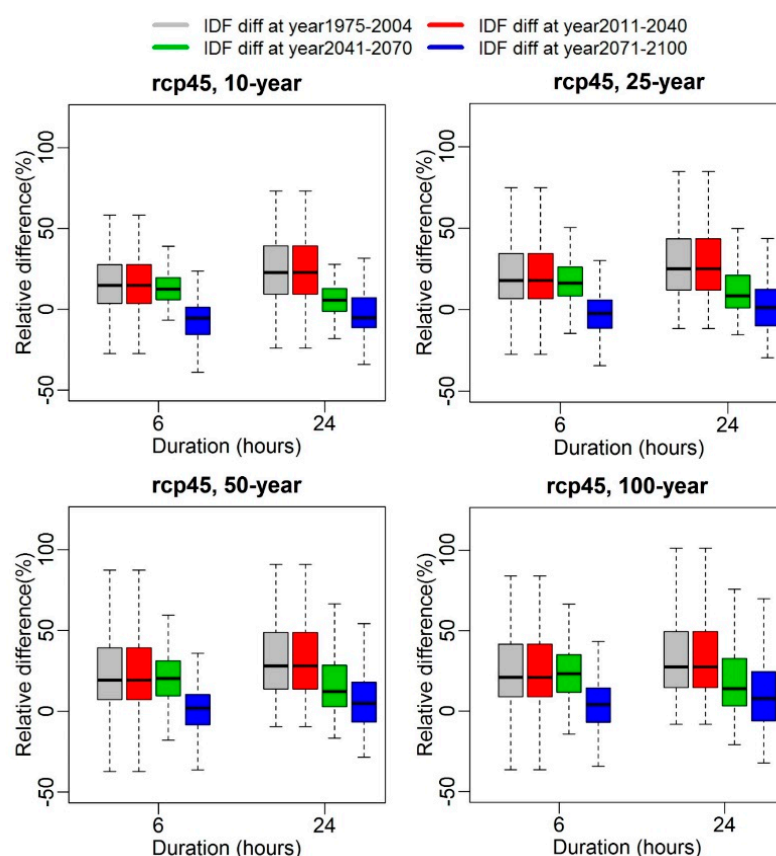
Figure 5. The relative differences of precipitation intensities from NEVA non-stationary IDF estimates to those from quasi-stationary IDF analysis, for the historical (1975–2004) and future time periods (2011–2040, 2041–2070, and 2071–2100), for 6- and 24-h duration events with 10-, 25-, 50-, and 100-year return periods, under the RCP4.5 scenario. Each boxplot corresponds to the distribution of estimated precipitation intensity differences across the grids of the entire watershed.
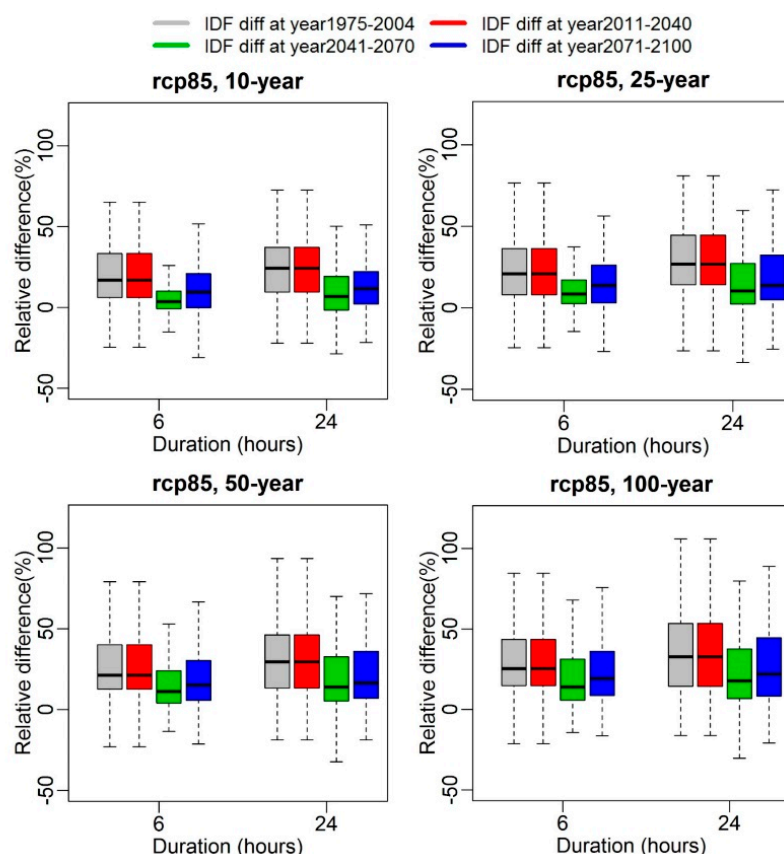
Figure 6. Same as Figure 5, but under the RCP8.5 scenario.

Geostatistical analysis was performed for 100-year precipitation intensities with durations of 6 and 24 h, respectively. Spatial maps were generated to illustrate the spatial distributions of such events under different climate scenarios. Figure 7 illustrates the spatial intensity distribution of 6-h 100-year events using both stationary and non-stationary IDF estimations. The spatial patterns during different quasi-stationary time periods vary with the changing climate. In general, the intensities are stronger in mountain regions located near the mid-west of the watershed for both stationary and non-stationary IDF analyses. Under the RCP4.5 scenario, the peak intensity is 20 mm/h from non-stationary IDF, which is about 8 mm/h (40%) or 4 mm/h (20%) higher compared to stationary historical and future IDFs respectively. The quasi-stationary time period 2041–2070 corresponds to a peak intensity of 20 mm/h near the southwest border of the watershed, which is 6 mm/h (30%) higher than from the non-stationary IDF. With the increasing carbon emission, the intensities increase as well. In the non-stationary IDF maps with lower carbon emission RCP4.5, two peak intensity areas can be identified. Under RCP8.5, one area near the middle of the watershed, with intensity over 18 mm/h, has twice as high a precipitation intensity as that under RCP4.5. Also, the northwest region shows a 30% increase in intensity from 16 mm/h to 20 mm/h. For the quasi-stationary time period of 2071–2100, the area has the largest peak intensity corresponding to the highest carbon emission.

Lastly, we note that for the precipitation pattern in a small watershed, the decadal variability can be rather significant. For RCP4.5, the precipitation intensity is strongest during 2041–2070, but for RCP8.5, the precipitation intensity is strongest during 2071–2100, suggesting a simple linear scaling of precipitation intensity changes with the global mean warming is not likely to work well. On the other hand, despite the decadal fluctuations, the spatial pattern of precipitation intensity is dominated by the topographic variations and remains similar throughout the historical and future periods.

The spatial intensity distribution maps of 24-h 100-year events from both stationary and non-stationary IDF estimations are shown in Figure 8. Compared to 6-h 100-year events, the

spatial patterns show some differences in both quasi-stationary and non-stationary IDF analyses. The west region of the watershed from the northern to the southern sides of the mountain forms a high intensity area that matches well with the terrain. The east side of the watershed with lower elevations has relatively weak intensities. The relationships between IDF curves and terrain/elevation were further evaluated, where the elevation for each numerical grid was extracted from the 3D Elevation Program (3DEP) provided by U.S. Geological Survey (USGS) [71]. The boxplot in Figure 9 displays the precipitation distribution for 6- and 24-h 100-year extreme events obtained by both quasi-stationary and non-stationary IDFs with elevations. The precipitation intensity increases with elevation in general.
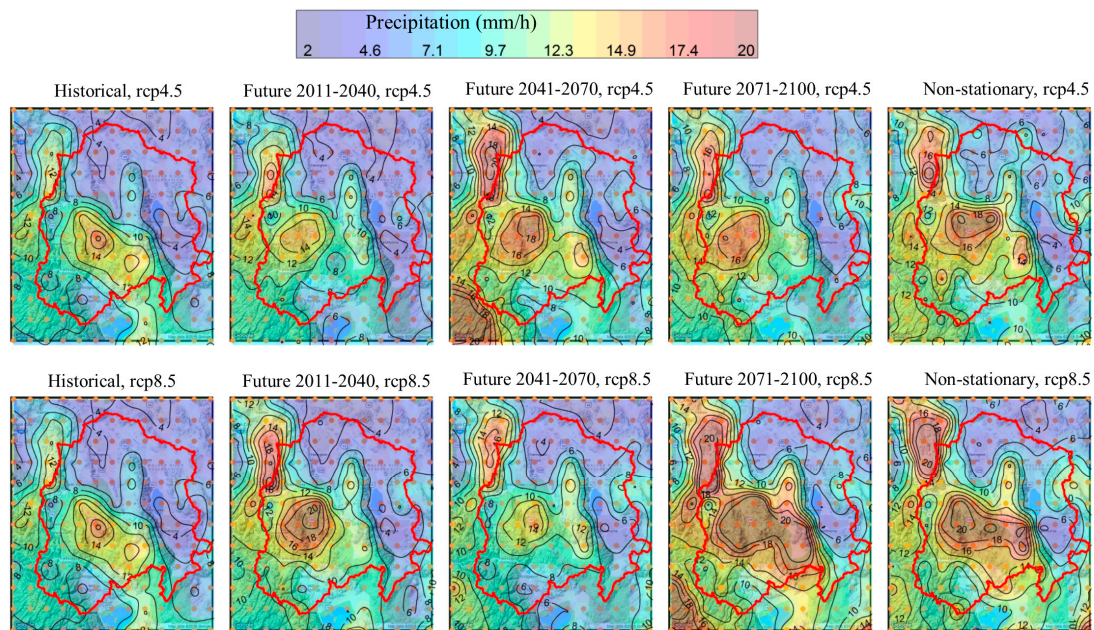
Figure 7. Spatial precipitation intensity distribution of 6-h duration 100-year events based on the quasi-stationary IDF approach for historical (1975–2004) and future (2011–2040, 2041–2070, and 2071–2100) time periods, and non-stationary estimation. The top row is for the RCP4.5 scenario; the bottom is for the RCP8.5 scenario.
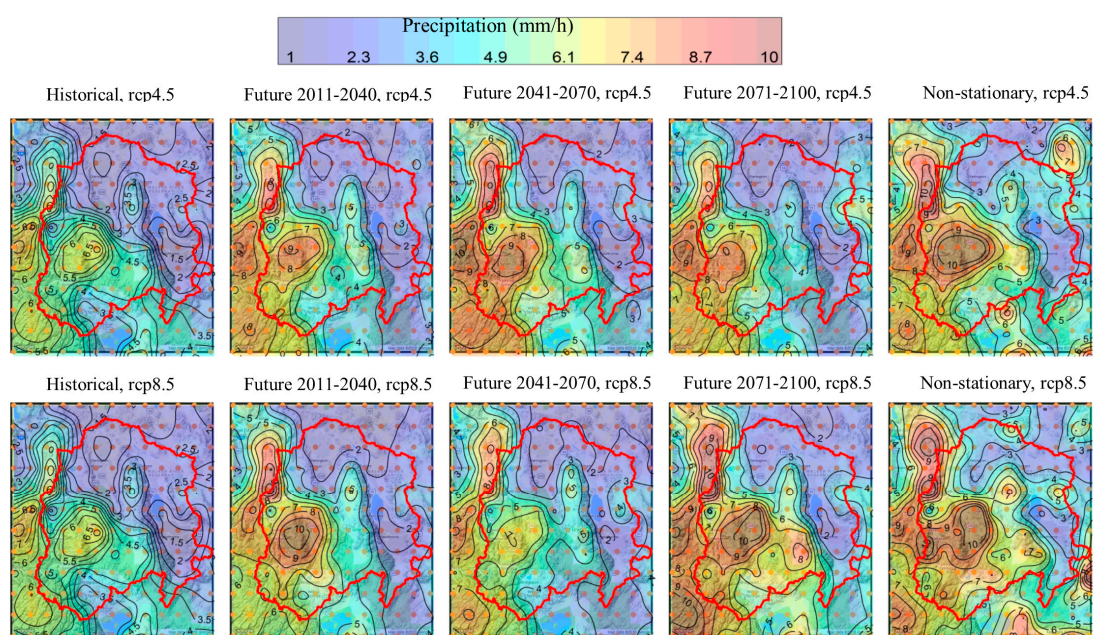
Figure 8. The same as Figure 7, but for 24-h duration events.
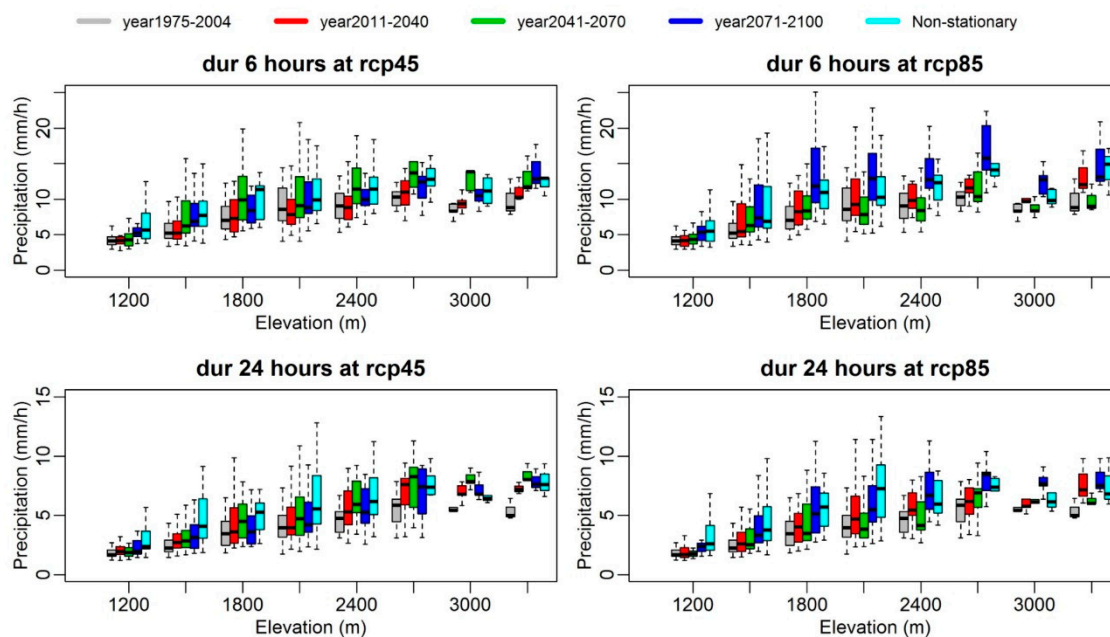
Figure 9. The boxplots of precipitation intensity for 6- and 24-h 100-year events at return period 100-year under different climate scenarios from the IDFs derived from quasi-stationary and non-stationary NEVA estimates, grouped by elevations of all the grids in the study domain.

When elevation increases from 1200 m to 3300 m, precipitation intensity may increase from 5 mm/h to 10 mm/h for the 6-h events; and it may increase from 3 mm/h to 7 mm/h for the 24-h events. Precipitation intensity is subject to larger variability under the higher carbon emission scenario. The spatial heterogeneity due to the terrain effect is comparable to but generally larger than the variability due to the impact of a changing climate. For example, for the spatial locations with an elevation around 1800 m, the historical IDF yields a 5–6 mm/h intensity, while the future quasi-stationary or non-stationary IDFs yield a 5–10 mm/h intensity (RCP4.5) or 6–12 mm/h intensity (RCP8.5).

4. Discussion and Conclusions

In this study, both quasi-stationary and non-stationary IDF analyses over the entire Walker watershed were carried out using 126-year precipitation AMS time series under two RCP future emission scenarios, with high spatiotemporal resolution (hourly, 0.125°) climate model outputs. Traditional IDFs obtained from six adjacent weather stations were used for comparison, suggesting that the bias-corrected precipitation generally reproduces the observations well, except at the station on the southwest corner of the watershed where large differences were noted for 6-h duration events. With uncertainties in the physics parameterizations of climate models and insufficient spatial resolution to capture important driving factors for the local climate, the use of climate simulations to develop IDFs may introduce biases and uncertainties.

Despite some limitations of the climate model outputs, the long time series of precipitation provided at relatively high resolution by the models have been useful for exploring different approaches to account for the effects of climate non-stationarity on IDF estimates. We find that the quasi-stationary IDFs for the future time window of 2071–2100 match the non-stationary IDFs quite well, but the traditional stationary assumption-based estimates deviate significantly from the two, due to the strong non-stationarity in the data. The quasi-stationary IDFs for the earlier quasi-stationary windows 1975–2004 and 2011–2040, generally have lower estimates of extreme precipitations, as expected. The terrain effect results in strong spatial heterogeneity in the extreme precipitation distribution, and such an effect is at least comparable to the non-stationarity effect on the IDF estimate of extreme precipitation.

Overall, our results show that the discrepancies among the three IDFs analyses due to non-stationarity are comparable to the spatial variabilities of the IDFs. This underscores a need to use an ensemble of non-stationary approaches to achieve unbiased and comprehensive IDF estimates. But both quasi- and non-stationary IDFs are better solutions than the traditional stationary approach as they incorporate information of the impacts of climate change on extreme precipitation in flood estimation. For a comprehensive hydrological infrastructure engineering design, both approaches may be considered to handle non-stationary data and incorporate the associated estimation uncertainties in risk analysis, in addition to using outputs from higher spatial resolution climate models (e.g., 4 km) to deal with spatial heterogeneity and/or ensemble climate models to address model uncertainty.

References

1. Watt, E.; Marsalek, J. Critical review of the evolution of the design storm event concept. *Can. J. Civ. Eng.* **2013**, *40*, 105–113. [CrossRef]
2. Endreny, T.A.; Imbeah, N. Generating robust rainfall intensity–duration–frequency estimates with short-record satellite data. *J. Hydrol.* **2009**, *371*, 182–191. [CrossRef]
3. Saghafian, B.; Golian, S.; Ghasemi, A. Flood frequency analysis based on simulated peak discharges. *Nat. Hazards* **2014**, *71*, 403–417. [CrossRef]
4. Eagleson, P.S. Dynamics of Flood Frequency. *Water Resour. Res.* **1972**, *8*, 878–898. [CrossRef]
5. Chow, V.T.; Maidment, D.R.; Mays, L.W. *Applied Hydrology*; McGraw-Hill: New York, NY, USA, 1988.
6. Chang, E.K.; Guo, Y.; Xia, X. CMIP5 multimodel ensemble projection of storm track change under global warming. *J. Geophys. Res. Atmos.* **2012**, *117*. [CrossRef]
7. Li, W.; Li, L.; Ting, M.; Liu, Y. Intensification of Northern Hemisphere subtropical highs in a warming climate. *Nat. Geosci.* **2012**, *5*, 830. [CrossRef]
8. Peck, A.; Prodanovic, P.; Simonovic, S.P. Rainfall Intensity Duration Frequency Curves Under Climate Change: City of London, Ontario, Canada. *Can. Water Resour. J.* **2012**, *37*, 177–189. [CrossRef]
9. Westra, S.; Fowler, H.; Evans, J.; Alexander, L.; Berg, P.; Johnson, F.; Kendon, E.; Lenderink, G.; Roberts, N. Future changes to the intensity and frequency of short-duration extreme rainfall. *Rev. Geophys.* **2014**, *52*, 522–555. [CrossRef]
10. Sarhadi, A.; Soulis, E.D. Time-varying extreme rainfall intensity-duration-frequency curves in a changing climate. *Geophys. Res. Lett.* **2017**, *44*, 2454–2463. [CrossRef]
11. Mailhot, A.; Duchesne, S.; Caya, D.; Talbot, G. Assessment of future change in intensity–duration–frequency (IDF) curves for Southern Quebec using the Canadian Regional Climate Model (CRCM). *J. Hydrol.* **2007**, *347*, 197–210. [CrossRef]
12. Sugahara, S.; Da Rocha, R.P.; Silveira, R. Non-stationary frequency analysis of extreme daily rainfall in Sao Paulo, Brazil. *Int. J. Clim.* **2009**, *29*, 1339–1349. [CrossRef]
13. Lima, C.H.R.; Kwon, H.H.; Kim, J.Y. A Bayesian beta distribution model for estimating rainfall IDF curves in a changing climate. *J. Hydrol.* **2016**, *540*, 744–756. [CrossRef]
14. Mondal, A.; Mujumdar, P.P. Modeling non-stationarity in intensity, duration and frequency of extreme rainfall over India. *J. Hydrol.* **2015**, *521*, 217–231. [CrossRef]
15. De Paola, F.; Giugni, M.; Topa, M.E.; Bucchignani, E. Intensity-Duration-Frequency (IDF) rainfall curves, for data series and climate projection in African cities. *SpringerPlus* **2014**, *3*, 133. [CrossRef] [PubMed]

16. Gilroy, K.L.; McCuen, R.H. A nonstationary flood frequency analysis method to adjust for future climate change and urbanization. *J. Hydrol.* **2012**, *414*, 40–48. [CrossRef]

17. Modesto Gonzalez Pereira, M.J.; Sanches Fernandes, L.F.; Barros Macário, E.M.; Gaspar, S.M.; Pinto, J.G.; Engineering, D. Climate change impacts in the design of drainage systems: Case study of Portugal. *J. Irrig. Drain. Eng.* **2014**, *141*, 05014009. [CrossRef]

18. Sanches Fernandes, L.; Pereira, M.; Morgado, S.; Macário, E. Influence of Climate Change on the Design of Retention Basins in Northeastern Portugal. *Water* **2018**, *10*, 743. [CrossRef]

19. Koutsoyiannis, D. Statistics of extremes and estimation of extreme rainfall: I. Theoretical investigation/Statistiques de valeurs extrêmes et estimation de précipitations extrêmes: I. Recherche théorique. *Hydrol. Sci. J.* **2004**, *49*. [CrossRef]

20. Koutsoyiannis, D.; Montanari, A. Negligent killing of scientific concepts: The stationarity case. *Hydrol. Sci. J.* **2015**, *60*, 1174–1183. [CrossRef]

21. De Luca, D.; Galasso, L. Stationary and non-stationary frameworks for extreme rainfall time series in southern Italy. *Water* **2018**, *10*, 1477. [CrossRef]

22. Serinaldi, F.; Kilsby, C.G. Stationarity is undead: Uncertainty dominates the distribution of extremes. *Adv. Water Resour.* **2015**, *77*, 17–36. [CrossRef]

23. Chan, S.C.; Kendon, E.J.; Fowler, H.J.; Blenkinsop, S.; Roberts, N.M.; Ferro, C.A. The value of high-resolution met office regional climate models in the simulation of multihourly precipitation extremes. *J. Clim.* **2014**, *27*, 6155–6174. [CrossRef]

24. Pavelko, M.T.; Orozco, E.L. *Hydrologic Data for the Walker River Basin, Nevada and California, Water Years 2010–14*; US Geological Survey: Reston, VA, USA, 2015; ISSN 2327-638X.

25. Gao, Y.; Leung, L.R.; Lu, J.; Liu, Y.; Huang, M.; Qian, Y.J.G.R.L. Robust spring drying in the southwestern US and seasonal migration of wet/dry patterns in a warmer climate. *Geophys. Res. Lett.* **2014**, *41*, 1745–1751. [CrossRef]

26. Kraucunas, I.; Clarke, L.; Dirks, J.; Hathaway, J.; Hejazi, M.; Hibbard, K.; Huang, M.; Jin, C.; Kintner-Meyer, M.; van Dam, K.K.J.C.C. Investigating the nexus of climate, energy, water, and land at decision-relevant scales: The Platform for Regional Integrated Modeling and Analysis (PRIMA). *Clim. Chang.* **2015**, *129*, 573–588. [CrossRef]

27. Skamarock, W.; Klemp, J.; Dudhia, J.; Gill, D.; Barker, D.; Dudha, M.; Huang, X.; Wang, W.; Powers, Y. *A Description of the Advanced Research WRF Version 3*; NCAR Technical Note; Mesoscale and Microscale Meteorology Division; National Center for Atmospheric Research: Boulder, CO, USA, 2008.

28. Lawrence, D.; Oleson, K.W.; Flanner, M.G.; Thorton, P.E.; Swenson, S.C.; Lawrence, P.J.; Zeng, X.; Yang, Z.-L.; Levis, S.; Skaguchi, K.; et al. Parameterization Improvements and Functional and Structural Advances in Version 4 of the Community Land Model. *J. Adv. Model. Earth Syst.* **2011**, *3*, 27. [CrossRef]

29. Gent, P.R.; Danabasoglu, G.; Donner, L.J.; Holland, M.M.; Hunke, E.C.; Jayne, S.R.; Lawrence, D.M.; Neale, R.B.; Rasch, P.J.; Vertenstein, M.; et al. The Community Climate System Model Version 4. *J. Clim.* **2011**, *24*, 4973–4991. [CrossRef]

30. Taylor, K.E.; Stouffer, R.J.; Meehl, G.A. An overview of CMIP5 and the experiment design. *Bull. Am. Meteorol. Soc.* **2012**, *93*, 485–498. [CrossRef]

31. Mann, H.B. Nonparametric Tests against Trend. *Econometrica* **1945**, *13*, 245–259. [CrossRef]

32. Pingale, S.M.; Khare, D.; Jat, M.K.; Adamowski, J. Spatial and temporal trends of mean and extreme rainfall and temperature for the 33 urban centers of the arid and semi-arid state of Rajasthan, India. *Atmos. Res.* **2014**, *138*, 73–90. [CrossRef]

33. Luo, Y.; Liu, S.; Fu, S.L.; Liu, J.S.; Wang, G.Q.; Zhou, G.Y. Trends of precipitation in Beijiang River basin, Guangdong Province, China. *Hydrol. Process.* **2008**, *22*, 2377–2386. [CrossRef]

34. Zhang, X.B.; Zwiers, F.W.; Li, G.L. Monte Carlo experiments on the detection of trends in extreme values. *J. Clim.* **2004**, *17*, 1945–1952. [CrossRef]

35. Patra, J.P.; Mishra, A.; Singh, R.; Raghuwanshi, N. Detecting rainfall trends in twentieth century (1871–2006) over Orissa State, India. *Clim. Chang.* **2012**, *111*, 801–817. [CrossRef]

36. Seleshi, Y.; Zanke, U. Recent changes in rainfall and rainy days in Ethiopia. *Int. J. Clim.* **2004**, *24*, 973–983. [CrossRef]

37. Yilmaz, A.; Perera, B. Extreme rainfall nonstationarity investigation and intensity–frequency–duration relationship. *J. Hydrol. Eng.* **2013**, *19*, 1160–1172. [CrossRef]

38. Agilan, V.; Umamahesh, N. Modelling nonlinear trend for developing non-stationary rainfall intensity–duration–frequency curve. *Int. J. Clim.* **2017**, *37*, 1265–1281. [CrossRef]

39. Sen, P.K. Estimates of the regression coefficient based on Kendall's tau. *J. Am. Stat. Assoc.* **1968**, *63*, 1379–1389. [CrossRef]

40. Da Silva, R.M.; Santos, C.A.; Moreira, M.; Corte-Real, J.; Silva, V.C.; Medeiros, I.C. Rainfall and river flow trends using Mann–Kendall and Sen's slope estimator statistical tests in the Cobres River basin. *Nat. Hazards* **2015**, *77*, 1205–1221. [CrossRef]

41. Partal, T.; Kahya, E. Trend analysis in Turkish precipitation data. *Hydrol. Process.* **2006**, *20*, 2011–2026. [CrossRef]

42. Donat, M.G.; Lowry, A.L.; Alexander, L.V.; O'Gorman, P.A.; Maher, N. More extreme precipitation in the world's dry and wet regions. *Nat. Clim. Chang.* **2016**, *6*, 508. [CrossRef]

43. Appel, U.; Brandt, A.V. Adaptive sequential segmentation of piecewise stationary time series. *Inf. Sci.* **1983**, *29*, 27–56. [CrossRef]

44. Michelangeli, P.-A.; Vautard, R.; Legras, B. Weather regimes: Recurrence and quasi stationarity. *J. Atmos. Sci.* **1995**, *52*, 1237–1256. [CrossRef]

45. Patel, A.P.; Timbadiya, P.; Patel, P. Development of IDF curves under non-stationary meteorological condition. In Proceedings of the 36th IAHR World Congress, The Hague, The Netherlands, 28 June–3 July 2015.

46. AghaKouchak, A.; Easterling, D.; Hsu, K.; Schubert, S.; Sorooshian, S. *Extremes in a Changing Climate: Detection, Analysis and Uncertainty*; Springer Science & Business Media: Berlin/Heidelberg, Germany, 2012; Volume 65.

47. Cheng, L.; AghaKouchak, A. Nonstationary precipitation intensity-duration-frequency curves for infrastructure design in a changing climate. *Sci. Rep.* **2014**, *4*, 7093. [CrossRef] [PubMed]

48. Cheng, L.Y.; AghaKouchak, A.; Gilleland, E.; Katz, R.W. Non-stationary extreme value analysis in a changing climate. *Clim. Chang.* **2014**, *127*, 353–369. [CrossRef]

49. Katz, R.W.; Parlange, M.B.; Naveau, P.J. Statistics of extremes in hydrology. *Adv. Water Resour.* **2002**, *25*, 1287–1304. [CrossRef]

50. Coles, S.; Bawa, J.; Trenner, L.; Dorazio, P. *An Introduction to Statistical Modeling of Extreme Values*; Springer: London, UK, 2001; Volume 208.

51. Melchers, R.E.; Beck, A.T. *Structural Reliability Analysis and Prediction*; John Wiley & Sons: Hoboken, NJ, USA, 2018.

52. Renard, B.; Sun, X.; Lang, M. Bayesian methods for non-stationary extreme value analysis. In *Extremes in a Changing Climate*; Springer: Dordrecht, The Netherlands, 2013; pp. 39–95.

53. Gilleland, E.; Katz, R.W. New software to analyze how extremes change over time. *Eostrans. Am. Geophys. Union* **2011**, *92*, 13–14. [CrossRef]

54. Shaw, E.M.; Beven, K.J.; Chappell, N.A.; Lamb, R. *Hydrology in Practice*; CRC Press: Boca Raton, FL, USA, 2010.

55. Bhagat, N. Flood Frequency Analysis Using Gumbel's Distribution Method: A Case Study of Lower Mahi Basin, India. *J. Water Resour. Ocean Sci.* **2017**, *6*, 51. [CrossRef]

56. Zelenhasic, E.F. *Theoretical Probability Distributions for Flood Peaks*; Hydrology Papers (Colorado State University); No. 42; Colorado State University: Fort Collins, CO, USA, 1970.

57. Sarma, P. Flood risk zone mapping of Dikrong sub basin in Assam. In Proceedings of the Map India 1999 Conference, New Delhi, India, 24–26 August 1999.

58. Ward, R. *Hydrology of Floods in Canada: A Guide to Planning and Design*; National Research Council Canada, Associate Committee on Hydrology: Ottawa, ON, Canada, 1989.

59. Solaiman, T.A.; Simonovic, S.P. *Development of Probability Based Intensity-Duration-Frequency Curves under Climate Change*; Department of Civil and Environmental Engineering, The University of Western Ontario City: London, ON, Canada, 2011.

60. Chow, V.T. Statistical and probability analysis of hydrologic data. In *Handbook of Applied Hydrology*; McGraw-Hill Book Company: New York, NY, USA, 1964; pp. 8.1–8.91.

61. Cheng, L. *Frameworks for Univariate and Multivariate Non-Stationary Analysis of Climatic Extremes*; UC Irvine: Irvine, CA, USA, 2014.

62. Katz, R.W. Statistics of extremes in climate change. *Clim. Chang.* **2010**, *100*, 71–76. [CrossRef]

63. Ragno, E.; AghaKouchak, A.; Love, C.A.; Cheng, L.; Vahedifard, F.; Lima, C.H.J. Quantifying changes in future intensity-duration-frequency curves using multimodel ensemble simulations. *Water Resour. Res.* **2018**, *54*, 1751–1764. [CrossRef]

64. Rosbjerg, D.; Madsen, H. Design with uncertain design values. In Proceedings of the International Conference on Hydrology in a Changing Environment, Exeter, England, 6–10 July 1998; pp. 155–163.

65. Ter Braak, C.J.; Vrugt, J.A. Differential evolution Markov chain with snooker updater and fewer chains. *Stat. Comput.* **2008**, *18*, 435–446. [CrossRef]

66. Ter Braak, C.J. A Markov Chain Monte Carlo version of the genetic algorithm Differential Evolution: Easy Bayesian computing for real parameter spaces. *Stat. Comput.* **2006**, *16*, 239–249. [CrossRef]

67. Vrugt, J.A.; ter Braak, C.J.F.; Diks, C.G.H.; Robinson, B.A.; Hyman, J.M.; Higdon, D. Accelerating Markov Chain Monte Carlo Simulation by Differential Evolution with Self-Adaptive Randomized Subspace Sampling. *Int. J. Nonlinear Sci. Numer. Simul.* **2009**, *10*, 273–290. [CrossRef]

68. Olea, R.A. *Geostatistics for Engineers and Earth Scientists*; Springer Science & Business Media: Berlin, Germany, 2012.

69. Isaaks, E.H.; Srivastava, R.M. *An Introduction to Applied Geostatistics*; Oxford University Press: New York, NY, USA, 1989.

70. Ribeiro, P.J., Jr.; Diggle, P.J. geoR: A package for geostatistical analysis. *R News* **2001**, *1*, 14–18.

71. Sugarbaker, L.J.; Constance, E.W.; Heidemann, H.K.; Jason, A.L.; Lukas, V.; Saghy, D.L.; Stoker, J.M. *The 3D Elevation Program Initiative: A Call for Action*; US Geological Survey: Reston, VA, USA, 2014; pp. 2330–5703.